Title

Optimization of K-edge imaging for vulnerable plaques using gold nanoparticles and energy resolved photon counting detectors: a simulation study

Permalink

https://escholarship.org/uc/item/2829r2hh

Journal

Physics in Medicine and Biology, 59(1)

ISSN

0031-9155

Authors

Alivov, Yahya
Baturin, Pavlo
Le, Huy Q
et al.

Publication Date

2014-01-06

DOI

10.1088/0031-9155/59/1/135

Copyright Information

Peer reviewed

Optimization of the K-edge imaging for vulnerable plaques using gold nanoparticles and energy-resolved photon counting detectors: a simulation study

Yahya Alivov[1], **Pavlo Baturin**, **Huy Q. Le**, **Justin Ducote**, and **Sabee Molloi**[2]
Department of Radiological Sciences, University of California, Irvine, California 92697

Abstract

We investigated the effect of different imaging parameters such as dose, beam energy, energy resolution, and number of energy bins on image quality of K-edge spectral computed tomography (CT) of gold nanoparticles (GNP) accumulated in an atherosclerotic plaque. Maximum likelihood technique was employed to estimate the concentration of GNP, which served as a targeted intravenous contrast material intended to detect the degree of plaque's inflammation. The simulations studies used a single slice parallel beam CT geometry with an X-ray beam energy ranging between 50 and 140 kVp. The synthetic phantoms included small (3 cm in diameter) cylinder and chest (33x24 cm^2) phantom, where both phantoms contained tissue, calcium, and gold. In the simulation studies GNP quantification and background (calcium and tissue) suppression task were pursued. The X-ray detection sensor was represented by an energy resolved photon counting detector (e.g., CdZnTe) with adjustable energy bins. Both ideal and more realistic (12% FWHM energy resolution) implementations of photon counting detector were simulated. The simulations were performed for the CdZnTe detector with pixel pitch of 0.5-1 mm, which corresponds to the performance without significant charge sharing and cross-talk effects. The Rose model was employed to estimate the minimum detectable concentration of GNPs. A figure of merit (FOM) was used to optimize the X-ray beam energy (kVp) to achieve the highest signal-to-noise ratio (SNR) with respect to patient dose. As a result, the successful identification of gold and background suppression was demonstrated. The highest FOM was observed at 125 kVp X-ray beam energy. The minimum detectable GNP concentration was determined to be approximately 1.06 µmol/mL (0.21 mg/mL) for an ideal detector and about 2.5 µmol/mL (0.49 mg/mL) for more realistic (12% FWHM) detector. The studies show the optimal imaging parameters at lowest patient dose using an energy resolved photon counting detector to image GNP in an atherosclerotic plaque.

I. Introduction

Most common coronary artery diseases (∼70 %) that lead to either fatal or non-fatal myocardial infarction are stenotic and vulnerable to rupture (Casscells *et al* 2003). These plaques have a large lipid core and a thin fibrous cap that can easily rupture and get lodged downstream in blood vessels, causing morbidity (Fayad and Fuster 2001). By contrast, severely stenotic plaques contain more smooth muscle cells and collagen, but smaller amounts of lipids and are less prone to rupture (MacNeill *et al* 2003). Identifying vulnerable plaques is an important step for the risk assessment of patients who are suspected to have coronary artery disease. Attempts to distinguish unstable plaques include techniques such as

---

[1]Corresponding author, e-mail address: yahya.alivov@colorado.edu. Currently at University of Colorado at Boulder, Boulder, CO, 80303.
[2]symolloi@uci.edu

intravascular ultrasound (IVUS) (Losordo *et al* 1994), IVUS elastography (de Korte et al 2000), angioscopy (Ueda *et al* 1996), optical coherence tomography (OCT) (Fujimoto *et al* 1999), spectroscopy (Raman (Brennan *et al* 1997), infra-red (Moreno *et al* 2002), fluorescence (Bosshart *et al* 1992)), intravascular magnetic resonance imaging (Fayad *et al* 2000), and computed tomography (CT) (MacNeill *et al* 2003). IVUS can visualize deep structures, but yields only 37% sensitivity for plaque rupture detection. IVUS elastography is based on the principle that tissue components with different hardness are expected to be compressed differently if a defined pressure is applied (Vavuranakis *et al* 1997). This technique can discriminate between soft and hard materials, assess the mechanical properties of the vessel wall, and detect lipid-rich and fibrous plaque (de Korte et al 2000). Angioscopy characterizes plaque composition and illuminates endoluminal irregularities, but the need to create a blood-free field limits its utility (Ueda *et al* 1996). The limitations of OCT are related to the features of a light-based energy source, including poor tissue penetration and interference from blood (MacNeill *et al* 2003). Vascular morphology along with the size and shape of the lipid content, obtained by the angioscopy procedure are helpful for estimating the grade of the stenosis but cannot determine the plaque's inflammatory status. Spectroscopy techniques are ideal for identifying the chemical composition of the tissue, but commonly have strong background fluorescence and are limited to *in vitro* studies ((Brennan *et al* 1997, Moreno *et al* 2002, Bosshart *et al* 1992). Magnetic resonance imaging (MRI) (Fayad *et al* 2000) and radionuclide imaging, such as single photon emission computed tomography (SPECT) or positron emission tomography (PET) (Gershlick *et al* 2007), can provide valuable functional information about plaque, but have suboptimal spatial resolution. They are also limited by the plaque's low tracer uptake and constant motion associated with heartbeat and respiration.

The multi-material discrimination task has become more feasible with the development of advanced CT methods such as dual energy imaging. This makes CT, which makes a CT modality preferable for imaging vulnerable plaque (Schoepf *et al* 2004, Schoenhagen *et al* 2004). CT is used to separate different tissues by exploiting its dependence on photoelectric and Compton scattering effects. Previous approaches to achieve this goal have been x-ray beam energy switching and multilayer detectors (Kalender 2006). However, these approaches use conventional energy integrating CT detectors. Also, both of these approaches lack the energy resolution inherent in integrating systems, there is a need for increased radiation airkerma, and the powerful monochromatic X-ray sources.

Emergence of a photon counting detector based on the CdZnTe systems (Fischer *et al* 2000, Lindner *et al* 2001) has enabled the development of spectral CT. Energy resolved photon counting detectors have a number of advantages over charge integrating detectors, which includes (1) possibility of detecting and counting each photon in the radiation beam, and (2) effectively rejecting electronic noise, Swank noise, and the afterglow effect. In addition to these benefits, photon counting detector potentially provides increased soft-tissue contrast, reduced radiation airkerma as well as beam-hardening effects (Roessl and Proksa 2007). While conventional energy integrating detectors often fail to differentiate between contrast-filled lumen and calcified plaque, the use of energy resolved photon counting detector can enable the possibility to differentiate between iodinated contrast material and calcification. This technique is especially promising for imaging the distribution of high Z elements in the human body by using X-ray attenuation measurements. This method was initially tested in a simulation study (Roessl and Proksa 2007), which showed it was possible to distinguish between calcified plaque and intravascular gadolinium chelate using additional spectral information. These predictions were experimentally proven in feasibility studies (Schlomka *et al* 2008). In this study a preclinical spectral CT scanner with a photon-counting detector and six energy threshold levels was used to scan a vessel phantom and to distinguish calcified plaque and gadolinium contrast material.

A contrast material should meet the following criteria: 1) physical characteristics that result in a higher value K-edge energy, 2) biocompatibility (little or non-toxicity), 3) high circulation time, and 4) high uptake by the targeted tissue. Since beam hardening effect causes the loss of photons from the low energy part of the spectrum, the detection of k-edge discontinuity in this region is limited due to photon starvation. Therefore, high Z elements are preferable since photon starvation issues are less severe. While iodine ($Z = 53$) seems to be a good candidate and is widely used in X-ray CT applications, it has a relatively low K-edge energy of 33.2 keV that makes it less practical for spectral K-edge imaging. Gadolinium ($Z = 64$) is frequently used as a contrast material in magnetic resonance imaging with a K-edge energy of 50.2 keV; so the photon starvation due to beam hardening is less severe as compared to that of iodine.

Gold nanoparticle (GNP) has been suggested for CT imaging since it meets most of these criteria (Kattumuri *et al* 2007, Hainfeld *et al* 2006, Boote *et al* 2010, Cai *et al* 2007). Gold (Au, Z=79) has a K-edge at 80.7 keV, which is good for K-edge imaging. Another advantage of GNPs is its minimal toxicity, which has been reported by a number of groups (Kattumuri *et al* 2007, Hainfeld *et al* 2006, Boote *et al* 2010, Cai *et al* 2007) This characteristic is very important since it provides potential for clinical applications. Also GNPs have a longer circulation time than iodinated contrast materials, and may provide enhanced signal contrast for a longer time after delivery to the patient (Cai *et al* 2007). For instance, PEG-coated GNPs have been reported to have up to 15 hours of circulation time (Cai *et al* 2007), which is significantly longer than that for iodine, which is less than 10 minutes. According to different research studies, the number of GNPs that a macrophage can uptake, ranges from 3×10^3 to 2×10^4, depending on the preparation conditions (Chithrani *et al* 2006, Wang *et al* 2009). The uptake of gold or other foreign nanoparticles by macrophages in the blood occurs by the actin-based mechanism called phagocytosis (Pratten *et al* 1986, Koval *et al* 1998). Since the human body may identify GNPs as foreign particles, gold nanoparticles has previously been coated with phytochemical gum-arabic matrix (Kattumuri *et al* 2007), polyethylene glycol (Cai *et al* 2007), and high-density lipoprotein (Au-HDL) that is specific for macrophages (Cormode *et al* 2008). Usage of Au-HDL nanoparticle not only improves gold nanoparticle uptake by plaques, but also further reduces possible toxicity issues. The advantage of this Au-HDL has previously been reported in animal studies (Cormode *et al* 2010).

In this work, we performed CT simulations of the detection and quantification of different concentrations of GNPs using an energy resolved photon counting detector. Effects of different CT parameters, such as airkerma, kVp, number of bins, and energy thresholds, on the quality of the reconstructed images were studied.

II. Methods

In this section, we introduce the theoretical background that was employed in simulations of GNP decomposition. Also we will provide details on phantom and simulation parameters.

A. Theory

After transmission through the matter, a polychromatic X-ray beam contains valuable information about the elemental composition of the absorber. There are two types of photon interaction with matter: photoelectric effect and Compton effect. While the Compton effect is the dominant interaction between X-ray photons and matter at higher energies, the photoelectric effect is the dominant interaction in the lower-energy domain of the spectrum. Separating the contributions of the Compton and photoelectric effect to X-ray attenuation is important for CT imaging. In the absence of K-edge discontinuities, the energy dependence of the linear attenuation coefficient $\mu(E, \overrightarrow{x})$ of materials is described by a linear

combination of the photoelectric and the Compton cross-sections $f_{ph}(E)$ and $f_{KN}(E)$ (Alvarez and Macovski 1976):

$$\mu(E, \overrightarrow{x})=a_{ph}(\overrightarrow{x})\frac{1}{E^3}a_{Co}(\overrightarrow{x})f_{KN}(E/E_e) \quad (1)$$

where $E_e \approx 511$ keV denotes the rest mass energy of the electron, the vector $\overrightarrow{x}$ describes the space dependence of the attenuation, and $f_{KN}(E)$ represents the energy dependent Klein-Nishina cross section. In the presence of high atomic number Z element with K-edge discontinuity, the equation describing the attenuation properties of matter is extended by the energy dependent attenuation function of this particular element as a third component (Lehmann *et al* 1981). In the case of gold (Au), the equation (1) becomes:

$$\mu(E, \overrightarrow{x})=a_{ph}(\overrightarrow{x})\frac{1}{E^3}+a_{Co}(\overrightarrow{x})f_{KN}(E/E_e)a_{Au}(\overrightarrow{x})f_{Au}(E)=\sum_{\alpha=1}^{3}a_\alpha(\overrightarrow{x})f_\alpha(E) \quad (2)$$

where ɑ= 1,2,3 represent the photoelectric, Compton, and contrast agent components, respectively. In the equation (3), $a_{Au}(\overrightarrow{x})$ and $f_{Au}(E)$ stand for local concentration and mass attenuation coefficient of gold. The mass attenuation coefficient of gold includes the photoelectric effect, Compton effect, and K-edge contributions of gold. In the case of an X-ray detector element that operates in energy resolved photon counting mode, the counting electronics allows the counting of each X-ray event into one of N adjacent energy bins B_i with $i = 1, \ldots, N$, according to the energy of the incoming photon. Assuming there is a perfect energy resolution in the absence of electronic noise, and noise resulting from incomplete charge collection in the sensor material, the expected value λ_i of the number of photons in the energy bin B_i can be related to the line-integrals A_α of the coefficients $a_\alpha(\overrightarrow{x})$:

$$\lambda_i(A_1, A_2, A_3)=\int_{\alpha=1}^{3}S_i(E)\Phi(E)\exp\left(-\sum f_\alpha(E)A_\alpha\right)D(E)dE, i=1,\ldots N, \quad (3)$$

where N is number of bins, and $A_\alpha \int a_\alpha(\overrightarrow{x})ds, \alpha=1, 2, 3$.

In this equation $\Phi(E)$ denotes the spectral X-ray photon fluence, $D(E)$ represents the detector absorption efficiency, and $S_i(E)$ are the sensitivities of various energy bins.

Equation 3 represents a system of N equations with three unknowns. Since the number of equations exceeds the number of unknowns (A_1, A_2, A_3), this system of equations is overdetermined and generally has no solution. This difficulty can be overcome by the maximum likelihood method (Nelder and Mead 1965), which is based on finding solutions of highest probability. In our case, this technique will be applied as follows: let $M_i(A_\alpha)$, i=1,2,…N, denote random variables describing the number of photons detected in the energy bins B_i, $\lambda_i(A_\alpha)$ represents the mean value, and both of these random variables and their corresponding means depend on the line-integrals $A_\alpha(A_1,A_2,A_3)$. Assuming that M_i forms a set of independent Poisson random variables, the likelihood function can be calculated as the probability of an arbitrary measurement result $(M_1 = m_1, \ldots, M_N = m_N)$ given a particular composition of the object parameterized by A_α:

$$P(m_{1,\ldots}m_N|\lambda_i(A_\alpha),\ldots.\lambda_N(A_\alpha))=\prod_{i=1}^{N}\frac{[\lambda_i(A_\alpha)]^{m_i}}{m_i!}\exp(-\lambda_i(A_\alpha)). \quad (4)$$

Instead of directly maximizing the likelihood function P, it is more convenient to minimize the negative log-likelihood L, which becomes the following after dropping terms independent of A_α:

$$L(m_1, \ldots m_N \mid \lambda_i(A_\alpha), \ldots \lambda_N(A_\alpha)) = -\ln[P(m_1, \ldots m_N \mid \lambda_i(A_\alpha), \ldots \lambda_N(A_\alpha))] \cong \sum_{i=1}^{N} \lambda_i(A_\alpha) - m_i \ln \lambda_i(A_\alpha) \quad (5)$$

The described maximum-likelihood framework is a pre-reconstruction technique, which is applied to the measured intensities in projection space, i.e. sinograms. It yields sinograms of photoelectric effect, Compton scattering, and concentration of gold. Furthermore, the filtered back projection reconstruction is used to generate CT slices of three basis images. The resulting image of the photoelectric process has a unit of $keV^3 \cdot cm^{-1}$, while the Compton image is expressed in the units of linear attenuation. The code values in the gold image correspond to the fractional concentrations of gold material used in the mixture.

B. CdZnTe detector

For the ideal detector, all photons were assumed to be detected (QDE=1.0), which means that statistical fluctuations of the pulse height for a given incident photon energy were neglected. For the clinical detector, the quantum detection efficiency was calculated by considering the photon absorption in a 3 mm thickness of $Gd_{1-x}Zn_xTe$ for x=0.1. CdZnTe crystals are fabricated from a mixture of CdTe and ZnTe by a crystal growing process, and are often specified as $Cd_{1-x}Zn_xTe$ to outline its composition, where indices $1-x$ and x indicate weight fractions of the CdTe and ZnTe components, respectively, used in the mixture. The CdZnTe crystals used in this study are x=0.1 and the weight fractions of Cd, Te, and Zn are 42%, 55%, and 3%, respectively. The atomic numbers of Cd and Te are 48 and 52, respectively, and the weight fractions of Cd and Te are also similar. The photon counting detector was assumed to operate in differential mode to obtain energy windows. The simulations were performed for the CdZnTe detector with pixel pitch of 0.5-1 mm. Most of the preclinical CdZnTe detectors have the pixel pitches in the order of 0.5 mm and larger (Schlomka et al 2008, Koenig et al 2012, Iwanczyk et al 2009, Ravi et al 2008). This detector condition corresponds to performance without significant degradation caused by charge sharing and cross-talk effects (Koenig et al 2012, Shikhaliev et al 2009). In particular, previous reports have shown that when pixel size increases from 100 μm to 1000 μm the number of characteristic x rays escaping the pixels and entering the neighboring pixel (cross-talk) decrease from 70% to 20% (Shikhaliev et al 2009). Furthermore, it has been shown that charge sharing can potentially be removed from the energy measurement when the chip is programmed in charge summing mode (Ballabriga et al 2013).

C. X-ray spectra

X-ray spectra for the simulation were computer-generated using a previously reported TASMIP model developed by Boone and Seibert (Boone and Seibert 1997). In this model, the X-ray tube spectra was calculated and parameterized for tungsten anode. The spectral model was incorporated into a Java program that could output a desired spectrum according to parameters such as x-ray tube target material, peak voltage, ripple fraction and beam filtration. Unless otherwise noted the beam energy was set to 120 kVp so that the photon flux was high enough for energies above 80.7 keV (the K-edge of gold). A beam energy of 120 kVp was used in simulations of material decomposition as a function of gold concentration, air kerma, and number of bins. The effect of beam energy on image quality was studied by varying it in the range 85-150 kVp. Figure 1 shows the X-ray spectrum produced during the simulations corresponding to 120 kVp. The detector pixels were equipped with $N=5$ different discriminator units, allowing a binning of the detected pulses

into five energy bins. A standard 2 mm aluminum filtration was used in simulation of the spectrum. The thresholds between energy bins are shown by vertical dashed lines (Figure 1). The bin thresholds (33, 49, 65, 80 and 120 keV) were set to take advantage of the K-edge of gold contrast agent and at the same time to provide the same number of photons in each energy bin. Specifically, bin five started just below the K-edge of gold (80.7 keV). The rest of the energy thresholds were chosen such that each bin contained almost equal number of counts. Although commercially available CdZnTe detectors (e.g., EV products) are equipped with 5 or 6 energy bins (Shikhaliev 2008, Schlomka *et al* 2008), the effect of the number of energy bins on GNP decomposition was also studied by varying the number of energy bins in the range 2-15.

Figure 2 presents the mass attenuation coefficients of gold, gadolinium, iodine, calcium, and tissue for comparison. The attenuation coefficients for various materials were obtained from previously reported data (Boone 1992). A sudden increase in the mass attenuation of gold μ_{Au} is observed near 80.7 keV, i.e. in the region of K-edge discontinuity. In contrast, mass attenuation coefficients of calcium μ_{Ca} (Figure 2, *curve 4)* and tissue μ_{tissue} (Figure 2, *curve 5)* are flat in this region of the spectrum, indicating a possibility of gold separation using K-edge of this material. Also, it is seen that the mass attenuation of gold is a factor of 8-10 greater than that of iodine. This means less gold is required to achieve the same linear attenuation coefficient (Figure 2).

D. Simulation parameters

The simulations were based on a single-slice parallel beam CT geometry. The program for decomposition was written in Matlab and it was based on the likelihood maximization method, as described above. Poisson noise was added to simulate statistical fluctuations in the measurement. The mean number of transmitted photons was computed for each discrete energy value between 1 keV and 150 keV at 1 keV increments. The measurement data for each of the energy bins was based on the calculated mean numbers of photons. The simulated photon counting data served as input for the maximum-likelihood pre-processing by providing images of the photoelectric and Compton cross-sections, as well as the local GNP concentration. The obtained images were analyzed using ImageJ software available on the National Institutes of Health web site (http://rsbweb.nih.gov/ij/). The limited energy resolution of the detector is expected to affect the GNP decomposition. Therefore, the blurring of the energy bin borders due to the limited energy resolution of the detector was also simulated. The energy resolution of the detector was estimated by FWHM of the detector up to 12%.

E. Phantoms

The CT simulation included 360 projections. The total dose was divided by 360 to estimate the dose deposited at each projection. Two different phantoms were used in the simulations. One was a 3-cm polymethylmethacrylate (PMMA) cylinder with a centrally-positioned 3-mm diameter tube surrounded by calcium, as shown in Figure 3a. The other phantom was a 33×24 cm^2 chest phantom, as shown in Figure 3b, which contained lungs, heart, muscle, and ribs with the sizes 7 cm, 10 cm, 6 cm, and 2 cm, respectively. While the small cylindrical phantom was used to demonstrate the method, the detailed simulations to study effects of beam energy, air kerma, number of bins, energy resolution and GNP concentration on reconstructed image quality were performed using the chest phantom. The concentration of calcium in the plaque was adjusted such that the linear attenuation coefficients of GNP and calcium were about the same, as can be seen from the charge-integrated image in Figure 3b. In this figure, GNP and calcium concentrations were 5.1 μmol/mL (1 mg/mL) and 250 μmol/mL (10 mg/mL), respectively. Such a choice of concentrations represents the worst case scenario where distinguishing between calcium and GNPs is difficult. The GNP

concentration during simulations varied in the range of 0.5-510 µmol/mL (0.1 - 20 mg/mL). In order to compare the minimum detectable concentration of the gold with that for iodine, a contrast agent widely used in X-ray imaging, simulations for iodine were also performed. This was done by replacing the gold in the chest phantom with iodine of different concentrations. The concentration of iodine was varied in the same range as that for gold (0.5–510 µmol/mL (0.1 - 20 mg/mL)).

F. Rose model

The effects of different imaging parameters, such as air kerma, beam energy, number of energy bins, and energy resolution, were studied on the mean value of decomposed Au concentration, contrast-to-noise ratio (CNR) and standard deviation (SD). CNR was calculated using:

$$CNR = \frac{|S_A - S_B|}{\sigma} \quad (6)$$

where S_A and S_B are signal intensities for GNP contrast agent and the background in the region of interest, respectively, σ is the standard deviation and represents the image noise. The standard deviation was calculated using ImageJ. Signal-noise ratio (SNR) was calculated using:

$$SNR = CNR \sqrt{N} \quad (7)$$

where N is the number of pixels in the area of interest. The Rose model's simple criteria for determining the detectability of contrast material as a function of concentration was implemented. The model is based on differentiating the target region from the background region. The basis for this differentiation is the differential number of detected photons between the two regions. This difference is expressed as the signal or signal difference to noise ratio. The equation for the Rose model is as follows [43]:

$$SNR^2 = CNR^2 \phi A \quad (8)$$

where SNR squared is equal to the product of the CNR squared, the photon fluence per unit area (φ) and the total area of the target region (A). A low contrast target is considered detectable when it has a SNR value greater than or equal to 5 (Hasegawa 2012).

G. kVp optimization

The X-ray beam energy (kVp) was optimized with respect to patient dose. One method to estimate patient dose is to use the entrance skin air kerma (ESAK) as a surrogate measure. After considering a wide range of beam energies and effects of beam filtration in this study, we found that the relation between patient dose to ESAK was not strong. Instead, the measure selected in this study was the air kerma, which is the total energy absorbed by the patient. This can be estimated by taking the difference between the energy of the incident beam and the energy of the beam after attenuation through the patient. In order to account for the energy loss from X-rays which scatter outside the patient, and therefore do not contribute to patient dose, a parameterized model of air kerma generated with data from Monte Carlo simulations was used (Boone 1992). A figure of merit (FOM) was chosen to optimize the SNR with respect to patient dose (Ducote 2011), and was defined as:

$$FOM = \frac{SNR}{\sqrt{AirKerma}} \quad (9)$$

This definition allows for image quality to be easily compared between the different configurations by taking the ratio of any two FOM's of interest. The air kerma was calculated for the incident spectra with beam energies ranging from 50-145 kVp in 5 keV increments. The total ESAK of 10.0 mGy and patient thickness of 30.0 cm was used. The dose at these conditions changed from 5 mGy to 15 mGy when kVp increased from 50 kVp to 145 kVp. The corresponding SNR for each kVp was estimated from analyzing reconstructed images after decomposition.

III. Results and Discussion

To demonstrate the K-edge gold decomposition method, the cylindrical phantom that consisted of gold, calcium, and tissue was initially used, as shown in Figure 3a. A total number of five bins were chosen to use the commercially available ASIC readout electronics with five independent input channels. The beam energy was chosen to be 120 kVp. Figure 4 shows the energy integrating **(a)**, Compton **(b)**, photoelectric **(c)**, and decomposed GNP **(d)** images. The photoelectric image (Figure 4c) shows the attenuation levels of the high-Z elements, except gold, since the photoelectric effect contribution of gold itself has already been accounted for in the gold based image (Figure 4d). The Compton image (Figure 4b) commonly depicts the electron concentration, which appears to be relatively homogeneous in our phantom.

While the cylinderical phantom was used for demonstrating the technique, the chest phantom was used for more detailed studies of the effects GNP concentration and other parameters on GNP detection. Figure 5 shows the effect of GNP concentration on the reconstructed image for the chest phantom. It is seen that while in the charge integrating image (Figure 5a) gold and calcium are undistinguishable after decomposition, only GNP remained in the reconstructed image (Figure 5 b, c) without any trace of tissue or calcium. For comparison, the image corresponding to 0.5 μmol/mL (0.1 mg/mL) GNP concentration is also shown (Figure 5 d) where no trace of GNP can be seen.

Figure 6 presents the mean value of Au concentration **(a)** and SNR **(b)** in the decomposed image as a function of the known GNP concentration for an ideal detector. A good consistency between known and calculated GNP densities can be seen from this figure. These results illustrate that the K-edge imaging method enables not only detection, but also quantification of the GNP contrast agent. The SNR increases almost linearly with an increase of GNP concentration. The minimum GNP concentration sufficient for detectability was estimated by the Rose model (SNR 5) and was equal to 1.06 μmol/mL (0.21 mg/mL). This is illustrated in Figure 6. For comparison, minimum detectable iodine concentration was also calculated replacing gold with iodine in the same chest phantom (Figure 3b), and the results are also plotted in Figure 6b along with the plot for gold. The estimated minimum detectable concentration for iodine was 5.1 μmol/mL (1 mg/mL).

The effect of air kerma on the GNP image quality was analyzed, and the results are shown in **Figure** 7. This figure presents dependence of GNP concentration **(a)** and CNR **(b)** as a function of air kerma. The range for airkerma was from 2 to 18 mGy. As seen from the Figure 7a, the calculated value of GNP concentration does not change significantly with air kerma and equals to the known value of 20.4 μmol/mL (4.02 mg/mL). However, the standard deviation appears higher for images corresponding to low air kerma. The CNR almost linearly increased with air kerma (Figure 7b).

The dependence of the decomposed GNP concentration and CNR on X-ray beam energy (kVp) is shown in Figure 8. The beam energy was varied from 85-150 kVp for a constant GNP concentration and air kerma, which were of 20.4 μmol/mL (4.02 mg/mL) and 15 mGy, respectively. As can be seen from the figure (Figure 8a), the mean value of GNP concentration is very close to the known value of 20.4 μmol/mL (4.02 mg/mL); however, the noise level increases with a decrease of beam energy. The CNR first increases with an increase of kVp, but later starts to saturate when kVp is higher than 100 kVp (Figure 8b). The saturation of CNR in this case can be explained by slow growth of number of photons in the X-ray spectrum with an increase of beam energy. For lower beam energy, the SD is higher, which can be explained by higher uncertainty coming from lower photon flux.

A figure of merit (FOM) was used to optimize the X-ray beam energy (kVp) in order to achieve the highest SNR with respect to patient dose. K-edge decomposition was performed for different beam energies, ranging from 40 kVp to 145 kVp in 5 kVp increments. The patient dose was maintained at 10 mGy during each simulation. The FOM was calculated using Equation 9. Figure 9 presents calculated FOM as a function of beam energy. It is seen that FOM first increases with beam energy and reaches maximum value at 125 kVp and then starts decreasing. These results indicate that the best beam energy for imaging gold in K-edge imaging is 125 kVp.

All above presented simulations were performed using five energy bins with equally spaced energy thresholds of 10, 32, 54, 76, and 99 keV. However, the effect of the number of energy bins (n) on CNR was also tested varying number of bins in the range of 2 -15. More specifically, the 120 kVp energy spectrum was divided into 2, 3, 5, 10 and 15 bins. For each number of bins, the energy threshold values were still chosen such that each of the energy bins would detect roughly the same amount of photons. The results of this analysis are shown in Figure 10. As it can be seen, the smaller number of bins results in smaller CNRs. However, at $n=5$, CNR starts to saturate and there is little improvement in CNR when bin number increases from 5 to 15.

The limited energy resolution of the detector is expected to affect the gold decomposition. Therefore, the blurring of the energy bin borders due to the limited energy resolution of the detector was simulated. The spectrum was divided into five energy bins, and the FWHM of energy resolution of the detector ranged from 2% to 12%. The results are presented in Figure 11. The mean value of the calculated GNP concentration, as a function of energy resolution, is shown in Figure 11. It is seen that the decomposed contrast agent concentration decreases with an increase of FWHM. For FWHM=12% the calculated GNP concentration was 2.5 μmol/mL (0.49 mg/mL), which was half of the known value 5.1 μmol/mL (1 mg/mL). This deviation can be explained by potential artifact of the maximum likelihood method; use of other reconstruction techniques may help to avoid such deviations (Ronaldson *et al.* 2012).

K-edge imaging was performed as a function of GNP concentration for the detector with an energy resolution of 12% and for X-ray spectrum with peak energy of 120 kVp, 5 energy bins, and 15 mGy airkerma. The resulting SNR as a function of GNP concentration is shown in Figure 12. Applying detectability threshold of Rose model (Hasegawa 2006) to this plot, the GNP detectability was found to be 2.5 μmol/mL (0.49 mg/mL). Therefore, as expected the minimum detectable GNP concentration for more realistic detector with 12% energy resolution was about twice higher than that for ideal detector (1.06 μmol/mL (0.21 mg/mL)). Similar to the case with ideal detector (Figure 6b), minimum detectable concentration for iodine was also calculated for the detector with FWHM=12% energy resolution and the results are presented in Figure 12b. The estimated minimum detectable concentration for iodine was 7.1 μmol/mL (0.87 mg/mL). This concentration was threefold higher than similar

parameter for gold. It would be interesting to compare the minimum detectable GNP concentration calculated for detector with 12% energy resolution (2.5 μmol/mL (0.49 mg/mL)) with that obtained from phantom studies. However, to the best of our knowledge, no systematic experimental studies were reported yet on minimum detectable GNP concentration. In recent studies by Cormode *et al.* several GNP concentrations were used in phantom studies with the lowest value 20 μmol/mL (4 mg/mL); the reconstructed gold K-edge image was clearly seen; however, no information was provided and no conclusions were made about the minimum detectable gold concentration (Cormode *et al* 2010). It should be noted that the noise level is sensor dependent that means different energy resolved photon counting detectors could exhibit different level of noise due to charge sharing and pulse pile up effects. Therefore, this factor has to be taken into account when comparing minimum detectable concentration.

The key features of the method presented in this work are: 1) use of energy resolved photon counting detector, and 2) use of GNPs with a K-edge in the high energy region of the X-ray spectrum (80.7 keV). However, a number of technological issues still need to be addressed before this method can be employed for clinical applications. While GNP toxicity, as was discussed above, is being overcome by covering GNP with bio-compatible materials (Kattumuri *et al* 2007, Cai *et al* 2007, Cormode *et al* 2008), a number of technical and engineering problems remain to be solved. Some of them include the count rate limitation of X-ray detectors due to charge sharing and pulse pile-up effects, long scanning time due to small field of view of available CZT detectors, and cupping and streak artifacts associated with the beam hardening have to be solved. In the simulations presented in this work the photon counting detector was considered free of pulse pile-up. However, pulse pile up is one of the major issues in photon counting detectors. In a conventional medical CT system with charge integrating detector photon fluxes as high as 10^8 photons/mm^2/sec are used, while the state-of-the art photon-counting detectors based on CZT or CdTe have the highest photon counting rate around 10^7 photons/mm^2/sec (Koenig *et al* 2012). Even with pile-up correction, there still remains a huge discrepancy between the count rates of these types of detectors. As one of the ways to overcome this problem sub-structuring of the pixels' anodes was proposed to reduce the count rate per pixel. However, when the pixel size reaches the size of the charge cloud produced by a stopped photon and its subsequent diffusion toward the anode, effects such as charge sharing, Compton scatter, and K-escape crosstalk become significant that spoil the spectral information. Therefore, it is important to develop correction techniques in the form of additional hardware or software to allow satisfactory spectral performance at these rates.

Simulations presented here were performed in a fan-beam geometry with only one detector line to accommodate the fact most of available commercial photon counting detectors use one line of detectors. However, all conventional CT systems with charge integrating detector use the cone-beam geometry. It is well known that scattered radiation is a significant issue in conventional CT to achieve high quality image. Therefore, methods have to be developed to address this issue. In addition, the dimensions of CZT detectors are typically small (a few centimeters), which limits the field of view and requires a helical scan and stitching, especially, for large objects. The offsets on sinograms associated with multi-section scans and stitching, and image distortions caused by interpolation in the helical reconstruction, can additionally complicate material decomposition.

The artifacts associated with beam-hardening effect is a serious problem because the gold is high Z material (Z=79) with high attenuation. Although the energy-resolving detectors have fewer beam-hardening related artifacts compared to conventional CT systems with charge integrating detector, it still can significantly impact the quality of material decomposition. If effective beam-hardening correction algorithm is not developed, the sensitivity of the

method will decrease due to these beam-hardening artifacts, resulting in increased detectable GNP concentration.

Thus, it is clear that there are many technical challenges to solve before photon-counting detectors and GNP K-edge imaging technique can be introduced into clinical practice.

Conclusion

We have performed simulations of material decomposition using GNPs and a spectral CT system and have shown the optimization of the technique for different imaging parameters. Simulation was performed for material decomposition based on the likelihood maximization method. The effect of different imaging parameters, such as GNP concentration, air kerma, beam energy and number of energy bins on CNR was studied. Also, the effect of energy resolution was studied on the image quality by varying the FWHM from 2% to 12%. The minimum detectable GNP concentration was found to be approximately 2.5 µmol/ml (0.49 mg/mL) for a detector with FWHM=12%.

Acknowledgments

References

Alvarez RE, Macovski A. Energy-Selective Reconstructions in X-Ray Computerized Tomography. Physics in Medicine and Biology. 1976; 21:733–744. [PubMed: 967922]

Ballabriga R, et al. The Medipix3RX: a high resolution, zero dead-time pixel detector readout chip allowing spectroscopic imaging. Journal of Instrumentation. 2013; 8

Boone JM. Parametrized X-Ray Absorption in Diagnostic-Radiology from Monte-Carlo Calculations - Implications for X-Ray-Detector Design. Medical Physics. 1992; 19:1467–1473. [PubMed: 1461211]

Boone JM, Seibert JA. Accurate method for computer-generating tungsten anode x-ray spectra from 30 to 140 kV. Medical Physics. 1997; 24:1661–1670. [PubMed: 9394272]

Boote E, et al. Gold Nanoparticle Contrast in a Phantom and Juvenile Swine: Models for Molecular Imaging of Human Organs using X-ray Computed Tomography. Academic Radiology. 2010; 17:410–417. [PubMed: 20207313]

Bosshart F. Fluorescence Spectroscopy for Identification of Atherosclerotic Tissue. Cardiovascular Research. 1992; 26:620–625. [PubMed: 1451142]

Brennan JF, et al. Determination of human coronary artery composition by Raman spectroscopy. Circulation. 1997; 96:99–105. [PubMed: 9236423]

Cai QY, et al. Colloidal gold nanoparticles as a blood-pool contrast agent for x-ray computed tomography in mice. Investigative Radiology. 2007; 42:797–806. [PubMed: 18007151]

Casscells W, et al. Naghavi M, Willerson JT. Vulnerable atherosclerotic plaque - A multifocal disease. Circulation. 2003; 107:2072–2075. [PubMed: 12719287]

Chithrani BD, et al. Determining the size and shape dependence of gold nanoparticle uptake into mammalian cells. Nano Letters. 2006; 6:662–668. [PubMed: 16608261]

Cormode DP, et al. Nanocrystal Core High-Density Lipoproteins: A Multimodality Contrast Agent Platform. Nano Letters. 2008; 8:3715–3723. [PubMed: 18939808]

Cormode DP, et al. Atherosclerotic Plaque Composition: Analysis with Multicolor CT and Targeted Gold Nanoparticles. Radiology. 2010; 256:774–782. [PubMed: 20668118]

Ducote, et al. Imaging of nanoparticles with dual-energy computed tomography. Physics in Medicine and Biology. 2011; 56:2031–2044. [PubMed: 21386141]

Fayad ZA, et al. Noninvasive in vivo human coronary artery lumen and wall imaging using black-blood magnetic resonance imaging. Circulation. 2000; 102:506–510. [PubMed: 10920061]

Fayad ZA, Fuster V. Clinical imaging of the high-risk or vulnerable atherosclerotic plaque. Circulation Research. 2001; 89:305–316. [PubMed: 11509446]

Fischer P, et al. A photon counting pixel chip with energy windowing. Ieee Transactions on Nuclear Science. 2000; 47:881–884.

Fujimoto JG, et al. High resolution in vivo intra-arterial imaging with optical coherence tomography. Heart. 1999; 82:128–133. [PubMed: 10409522]

Gershlick AH, et al. Role of non-invasive imaging in the management of coronary artery disease: an assessment of likely change over the next 10 years. A report from the British Cardiovascular Society Working Group. Heart. 2007; 93:423–431. [PubMed: 17401065]

Hainfeld JF, et al. Gold nanoparticles: a new X-ray contrast agent. British Journal of Radiology. 2006; 79:248–253. [PubMed: 16498039]

Hasegawa, B., et al. The Physics of Medical X-Ray Imaging. Medical Physics Publishing Company; Madison, Wisconsin:

Iwanczyk JS, et al. Photon Counting Energy Dispersive Detector Arrays for X-ray Imaging. IEEE Transactions on Nuclear Science. 2009; 56:535–542. [PubMed: 19920884]

Kalender WA. X-ray computed tomography. Physics in Medicine and Biology. 2006; 51:R29–R43. [PubMed: 16790909]

Kattumuri V, et al. Gum arabic as a phytochemical construct for the stabilization of gold nanoparticles: In vivo pharmacokinetics and X-ray-contrast-imaging studies. Small. 2007; 3:333–341. [PubMed: 17262759]

Koenig T, et al. Zwerger A, Fauler A, Fiederle M, Oelfke U. Imaging properties of small-pixel spectroscopic x-ray detectors based on cadmium telluride sensors. Physics in Medicine and Biology. 2012; 57:6743–6759. [PubMed: 23032372]

de Korte CL, et al. Characterization of plaque components and vulnerability with intravascular ultrasound elastography. Physics in Medicine and Biology. 2000; 45:1465–1475. [PubMed: 10870704]

Koval M, et al. Size of IgG-opsonized particles determines macrophage response during internalization. Experimental Cell Research. 1998; 242:265–273. [PubMed: 9665824]

Lehmann LA, et al. Generalized Image Combinations in Dual Kvp Digital Radiography. Medical Physics. 1981; 8:659–667. [PubMed: 7290019]

Lindner M, et al. Medical X-ray imaging with energy windowing. Nuclear Instruments & Methods in Physics Research Section a-Accelerators Spectrometers Detectors and Associated Equipment. 2001; 465:229–234.

Losordo DW, et al. Focal Compensatory Enlargement of Human Arteries in Response to Progressive Atherosclerosis - in-Vivo Documentation Using Intravascular Ultrasound. Circulation. 1994; 89:2570–2577. [PubMed: 8205666]

MacNeill BD, et al. Intravascular modalities for detection of vulnerable plaque - Current status. Arteriosclerosis Thrombosis and Vascular Biology. 2003; 23:1333–1342.

Moreno PR, et al. Detection of lipid pool, thin fibrous cap, and inflammatory cells in human aortic atherosclerotic plaques by near-infrared spectroscopy. Circulation. 2002; 105:923–927. [PubMed: 11864919]

Nelder JA, Mead R. A Simplex-Method for Function Minimization. Computer Journal. 1965; 7:308–313.

Pratten MK, Lloyd JB. Pinocytosis and Phagocytosis - the Effect of Size of a Particulate Substrate on Its Mode of Capture by Rat Peritoneal-Macrophages Cultured Invitro. Biochimica Et Biophysica Acta. 1986; 881:307–313. [PubMed: 3008849]

Ravi A, et al. Experimental evaluation of an online gamma-camera imaging of permanent seed implantation (OGIPSI) prototype for partial breast irradiation. Medical Physics. 2008; 35:2485–2492. [PubMed: 18649481]

Roessl E, Proksa R. K-edge imaging in x-ray computed tomography using multi-bin photon counting detectors. Physics in Medicine and Biology. 2007; 52:4679–4696. [PubMed: 17634657]

Ronaldson JP, et al. Toward quantifying the composition of soft tissues by spectral CT with Medipix3. Medical Physics. 2012; 39:6847–6857. [PubMed: 23127077]

Schlomka JP, et al. Experimental feasibility of multi-energy photon-counting K-edge imaging in preclinical computed tomography. Physics in Medicine and Biology. 2008; 53:4031–4047. [PubMed: 18612175]

Schoenhagen P, et al. Noninvasive imaging of coronary arteries: Current and future role of multi-detector row CT. Radiology. 2004; 232:7–17. [PubMed: 15220490]

Schoepf UJ, et al. CT of coronary artery disease. Radiology. 2004; 232:18–37. [PubMed: 15220491]

Shikhaliev PM. Energy-resolved computed tomography: first experimental results. Physics in Medicine and Biology. 2008; 53:5595–5613. [PubMed: 18799830]

Shikhaliev PM, et al. Photon counting multienergy x-ray imaging: Effect of the characteristic xrays on detector performance. Medical Physics. 2009; 36:5107–5119. [PubMed: 19994521]

Ueda Y, et al. Intracoronary morphology of culprit lesions after reperfusion in acute myocardial infarction: Serial angioscopic observations. Journal of the American College of Cardiology. 1996; 27:606–610. [PubMed: 8606271]

Vavuranakis M, et al. Impaired compensatory coronary artery enlargement in atherosclerosis contributes to the development of coronary artery stenosis in diabetic patients - An in vivo intravascular ultrasound study. European Heart Journal. 1997; 18:1090–1094. [PubMed: 9243141]

Wang B, et al. Plasmonic Intravascular Photoacoustic Imaging for Detection of Macrophages in Atherosclerotic Plaques. Nano Letters. 2009; 9:2212–2217. [PubMed: 18844426]
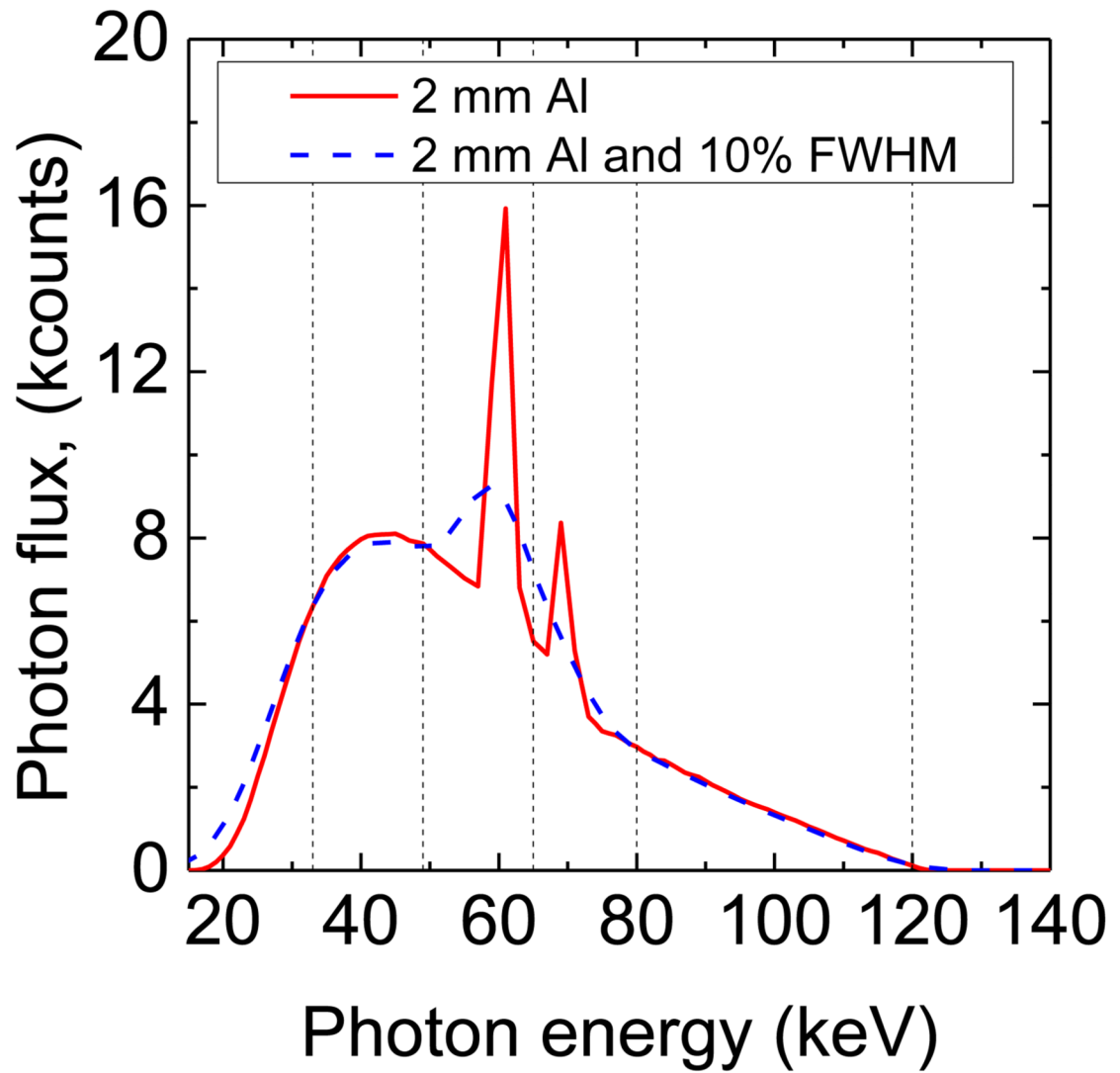
Figure 1.
X-ray spectra generated by TASMIP code using 120 kVp and tungsten anode: solid red line
with 2 mm Al filtration, dotted blue line with 2 mm Al filtration and 12% energy blurring.
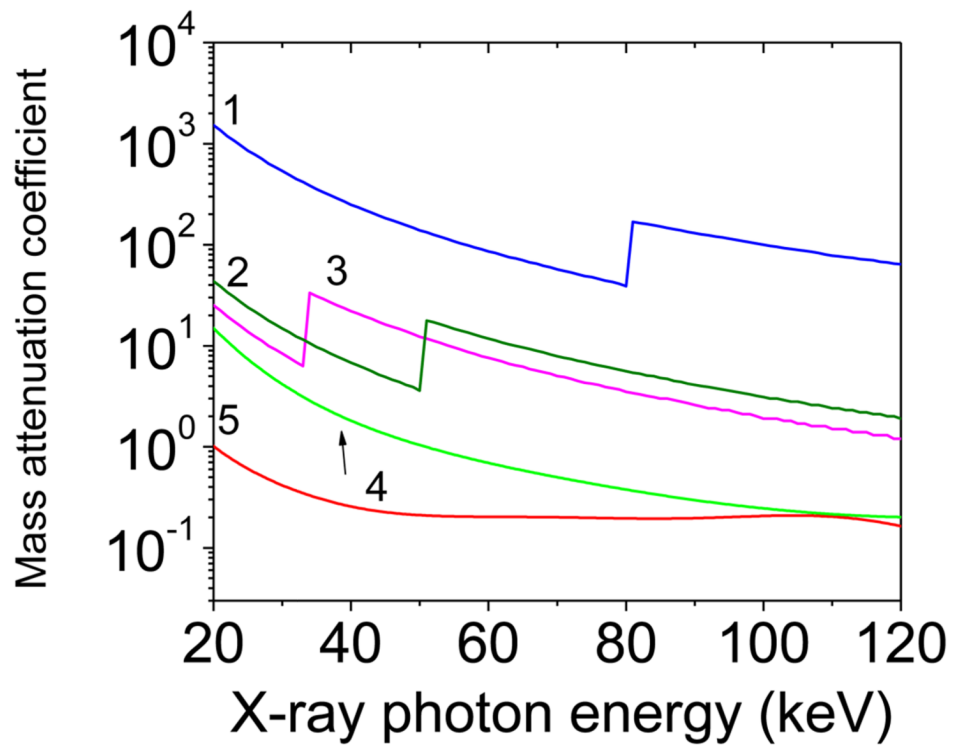
Figure 2.
Mass attenuation coefficients of gold (curve 1), gadolinium (curve 2), iodine (curve 3), calcium (curve 4), and tissue (curve 5)
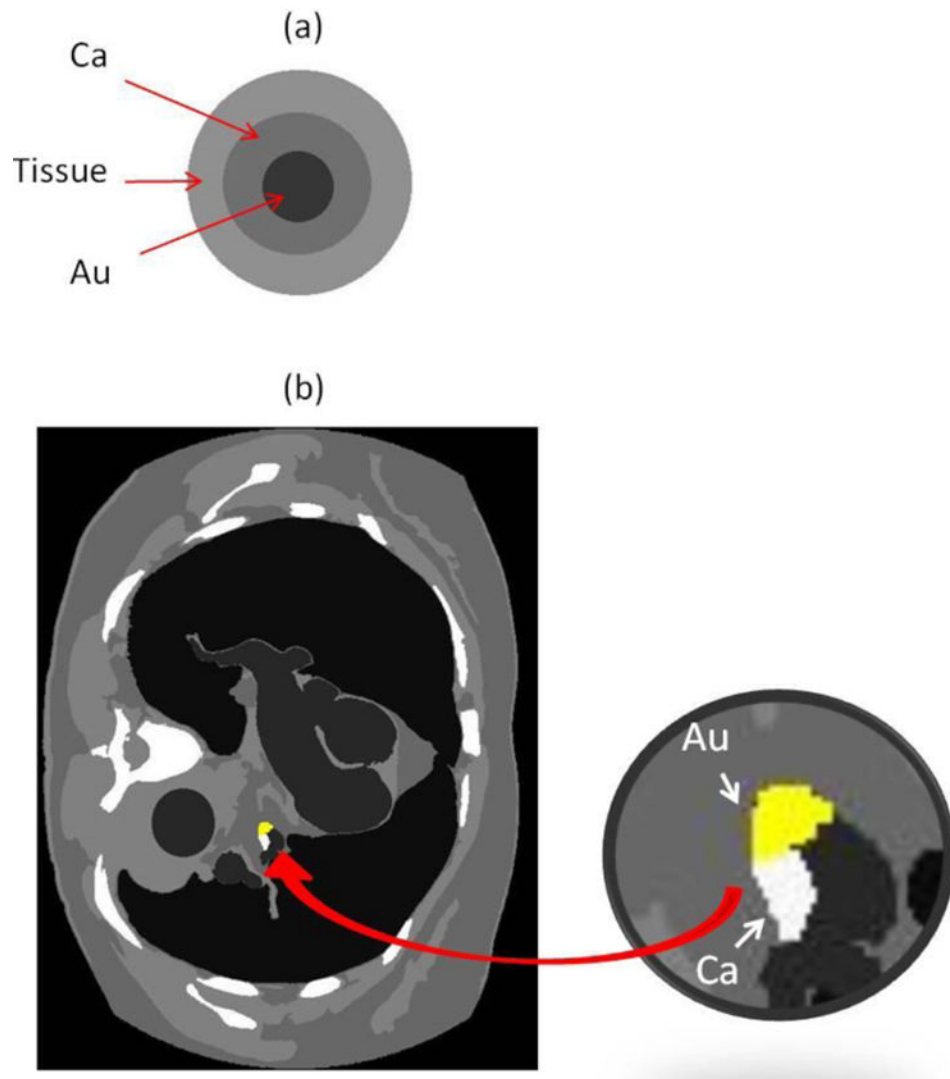
Figure 3.
Phantoms used in simulations: (a) PMMA phantom with a centrally-positioned 3-mm diameter cylinder surrounded by calcium; (b) chest phantom with magnified area of the plaque. The size of the chest phantom was 33×24 cm^2 and contained lungs, heart, muscle, and ribs with the sizes 7 cm, 10 cm, 6 cm, and 2 cm, respectively.
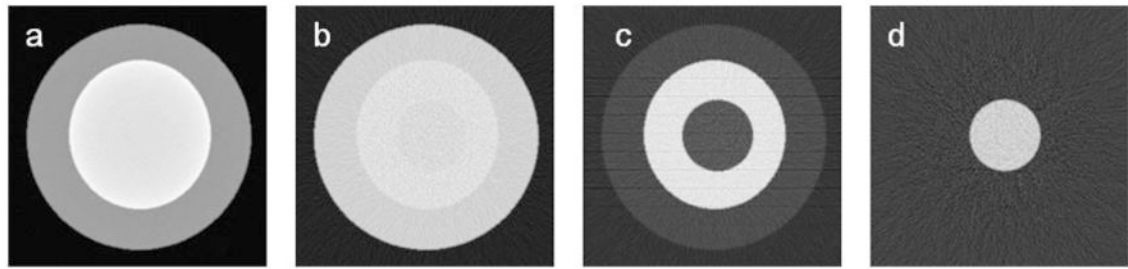
Figure 4.
Charge integrating (a), Compton (b), photoelectric (c), and decomposed GNP (d) images of a cylindrical PMMA phantom with a centrally-positioned 3-mm diameter tube surrounded by calcium.
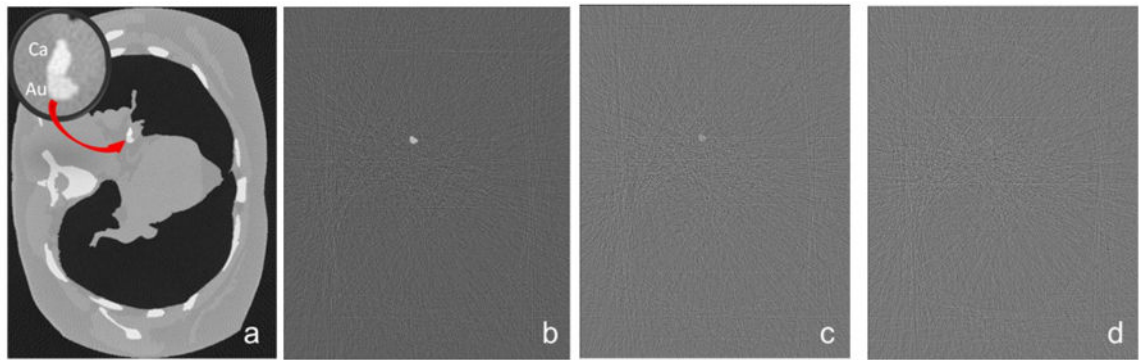
Figure 5.
Image of the chest phantom (a) and the decomposed GNP images at different concentrations: (b) 5.1 µmol/ml (1 mg/mL), (c) 1.5 µmol/ml (0.3 mg/mL), and (d) 0.5 µmol/ml (0.1 mg/mL).
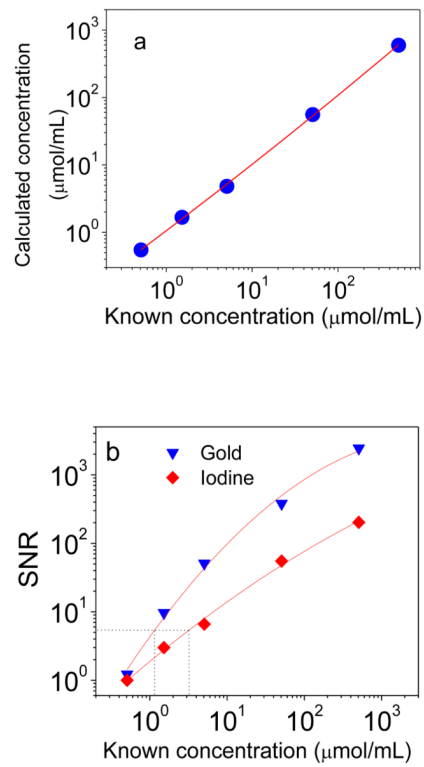
Figure 6.
(a) Calculated versus known concentration of GNP. (b) SNR for GNP and iodine as a function of contrast material concentration. These calculations correspond to an ideal detector. The minimum detectable GNP concentration determined using Rose model was 1.06 μmol/mL (0.21 mg/mL) for gold, and 5.1 μmol/mL (0.63 mg/mL) for iodine.
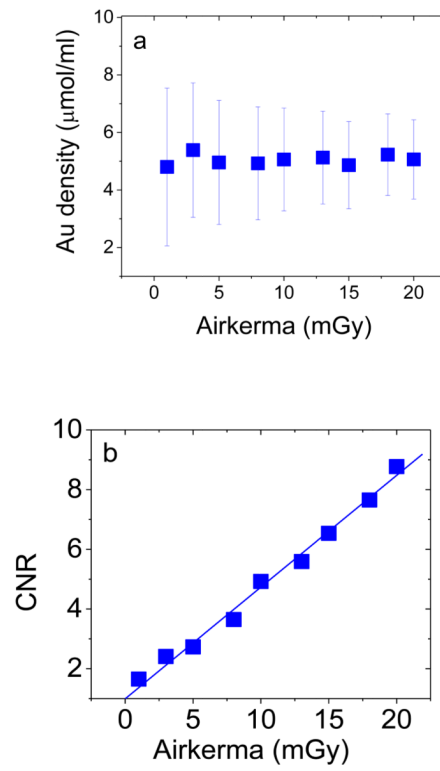
Figure 7.
(a) Decomposed GNP concentration and (b) CNR as a function of dose. The GNP concentration during simulations was 5.1 µmol/ml (1 mg/mL).
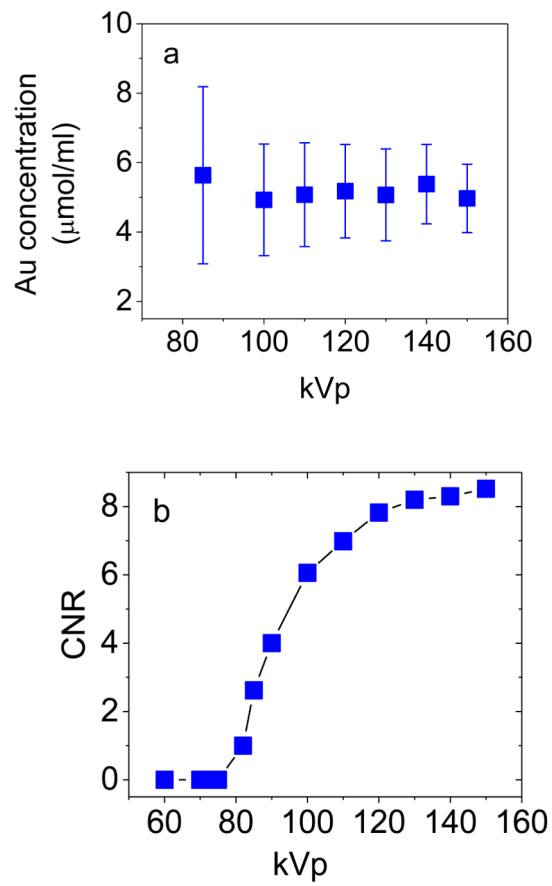
Figure 8.
(a) Decomposed GNP concentration and (b) CNR as a function of beam energy (kVp).
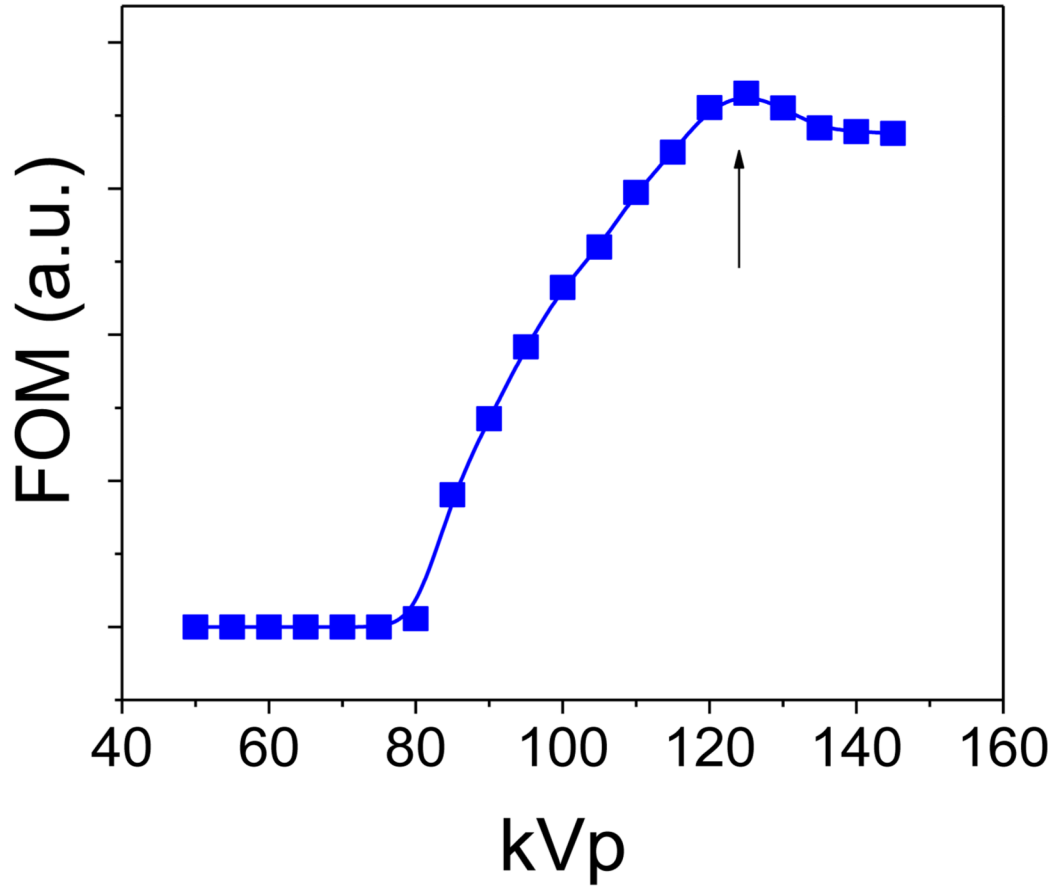
Figure 9.
Normalized FOM as a function of X-ray beam energy (kVp). The arrow in the figure points to the FOM with the highest value, which was near 125 kVp.
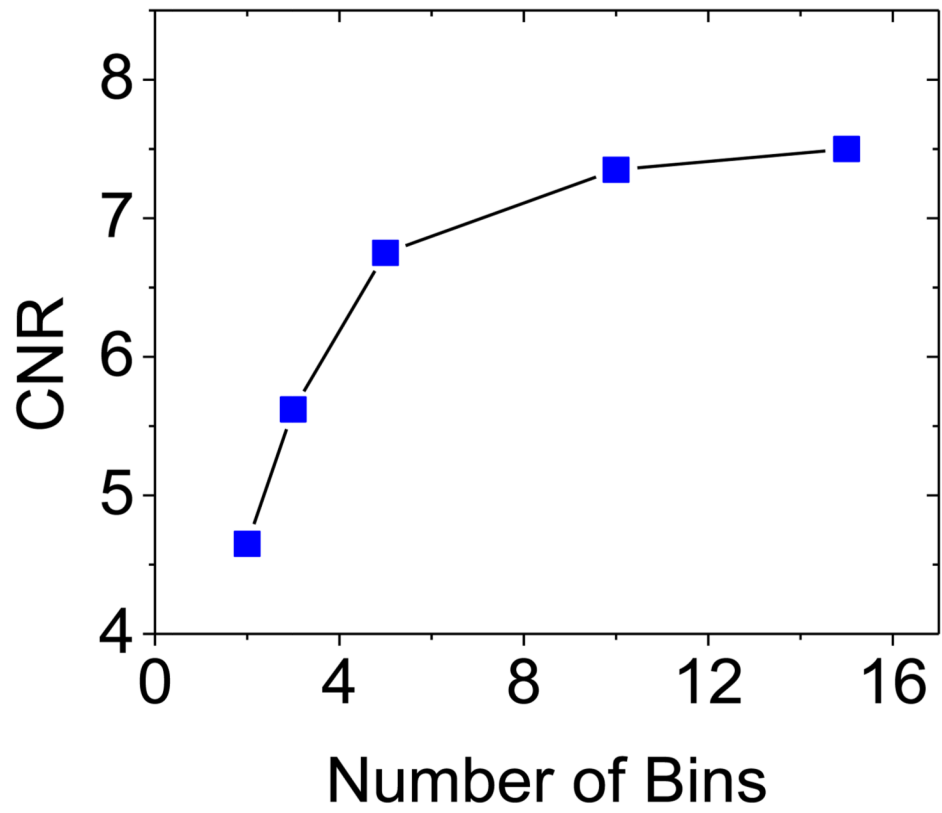
Figure 10.
CNR as a function of number of bins. 2-15 energy bins were used during the simulation.
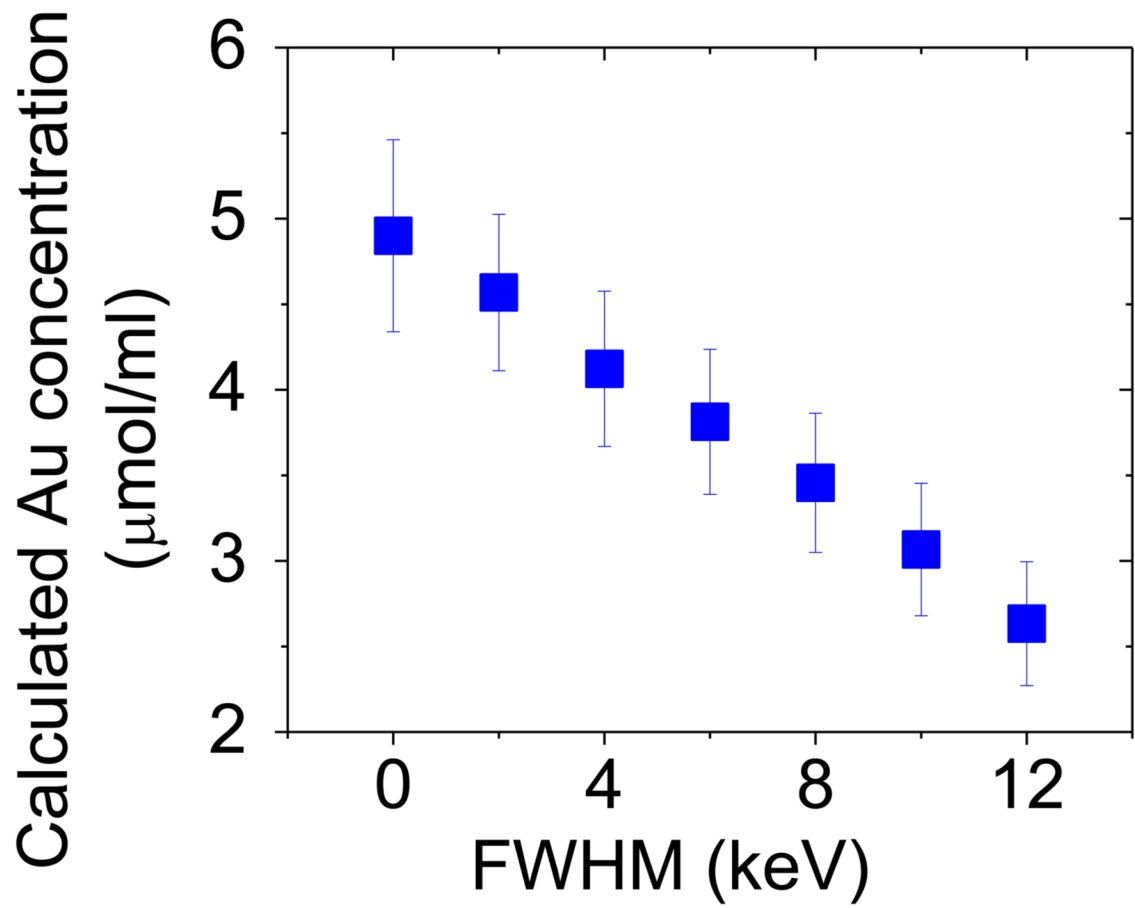
Figure 11.
Calculated GNP concentration for detector with various energy resolutions (FWHM). The calculations were performed for GNP of concentration 5.1 µmol/ml (1 mg/mL).
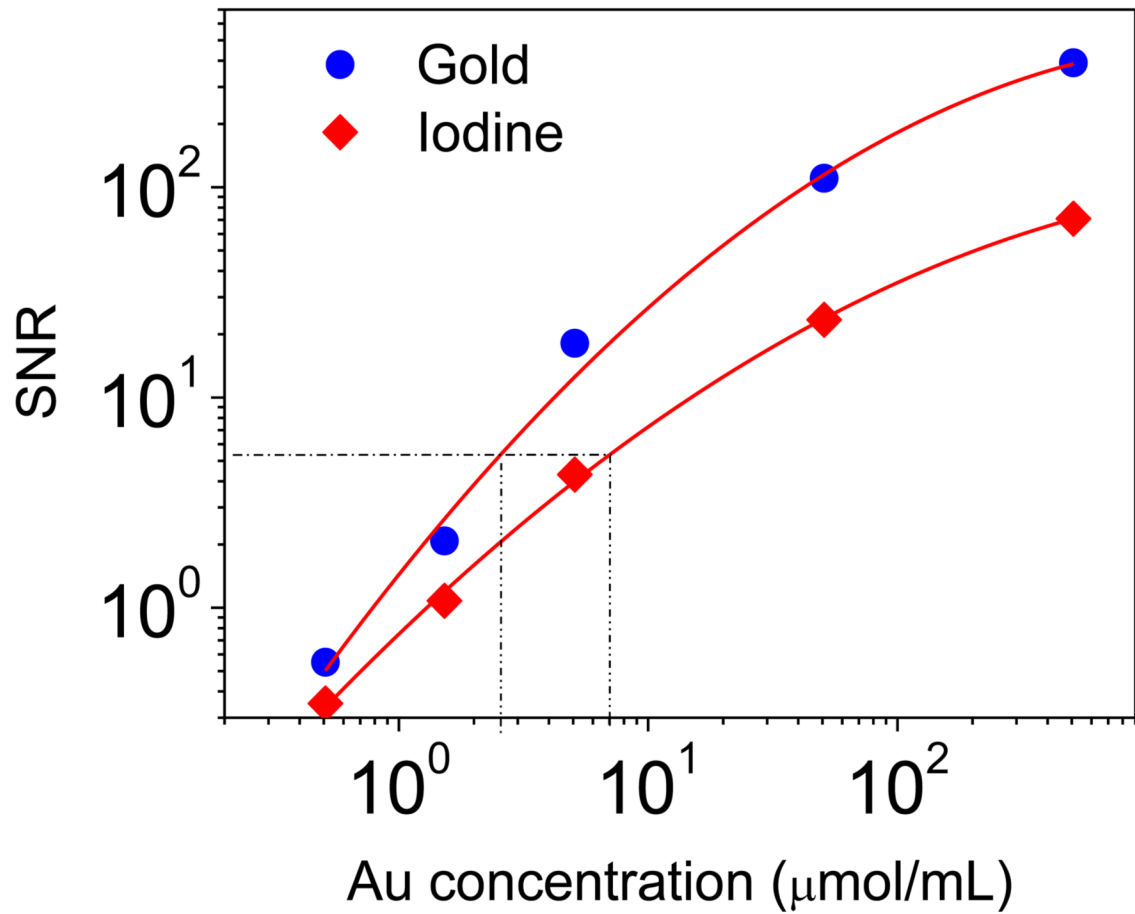
Figure 12.
SNR of decomposed GNP and iodine as a function of known concentration calculated for detector with energy resolution of 12%. The minimum detectable concentration determined using Rose model was 2.5 µmol/mL (0.49 mg/mL) for GNP, and 7.1 µmol/mL (0.87 mg/mL) for iodine